Glare Pattern Depiction: High-Fidelity Physical Computation and Physiologically-Inspired Visual Response - Supplementary Materials

YUXIANG SUN* and GLADIMIR V. G. BARANOSKI, University of Waterloo, Canada

This supplementary material provides additional information that could not be included in the main paper due to space constraints. It contains:

- a derivation of the diffraction formulas adopted in prior work,
- a detailed derivation of the final visual response function,
- implementation details relevant to our simulation framework,
- a discussion of the computational efficiency of the offline diffraction propagation,
- a set of reference images of the glare phenomenon captured by a camera, and
- a demonstration of how different light sources influence the glare pattern.

S1 Diffraction Equations

While the main text of this article presents the final formula for diffraction propagation (Section 3.2), this supplementary section provides additional derivation details and discusses the underlying connections.

S1.1 Rayleigh-Sommerfeld Diffraction Theory

Under the scalar diffraction theory and finite aperture boundary conditions (*i.e.*, a finite aperture size), the Rayleigh-Sommerfeld (RS) diffraction solution provides an approximate monochromatic solution to Maxwell's equations, which can be expressed as [Goodman 2017]:

$$U(x_i, y_i, z_i) = \frac{z_i}{2\pi} \iint_P U(x_p, y_p, 0) \left(\frac{1}{r} - jk\right) \frac{e^{jkr}}{r^2} dx_p dy_p, \tag{S1a}$$

$$r = \sqrt{z_i^2 + (x_i - x_p)^2 + (y_i - y_p)^2}, \tag{S1b}$$

where $(x_p, y_p, z_p = 0)$ and (x_i, y_i, z_i) are points on the pupil plane and image plane, respectively, $U(x, y, z)$ is the complex amplitude that encodes the amplitude and phase of a wave at a specific point, λ is the wavelength, $k = \frac{2\pi}{\lambda}$ is the wave vector and $P(x, y)$ is the mask representation of pupil or obstacle at position (x, y). We note that j is used to represent the imaginary unit.

The RS diffraction integral can be solved through the convolution theorem (Eq. S2), which states that the Fourier transform of the convolution of two functions is the product of their Fourier transform [Goodman 2017]:

$$\mathcal{F}\left[\iint u(x, y) v(x - \xi, y - \eta) dx dy\right] = \mathcal{F}[u(x, y)]\mathcal{F}[v(x, y)], \tag{S2}$$

*Corresponding author

Authors' Contact Information: Yuxiang Sun; Gladimir V. G. Baranoski, University of Waterloo, Waterloo, Canada.

where $\mathcal{F}, \mathcal{F}^{-1}$ are the Fourier transform and its inverse. By defining u and v as:

$$u(x_p, y_p, z_p) = U(x_p, y_p, z_p), \tag{S3a}$$

$$v(x_i, y_i, z_i) = \frac{z_i}{2\pi}\left(\frac{1}{r} - jk\right)\frac{e^{jkr}}{r^2}, r = \sqrt{z_i^2 + x_i^2 + y_i^2}, \tag{S3b}$$

the integral part of RS (Eq. S1) could be written as a convolution:

$$U(x_i, y_i, z_i) = \mathcal{F}^{-1}(\mathcal{F}(u)\mathcal{F}(v)). \tag{S4}$$

Although the convolution solution expressed in Eq. S4 is accurate, it is computationally expensive as we will show in Section S4. Thus, multiple diffraction approximations exist based on the light propagation distance. In the remainder of this section, we will briefly review some of these approximations relevant to our simulations.

S1.2 Ochoa's Approximation

Ochoa [2017] proposes that, for circular apertures, the distance r (Eq.S1b) can be approximated as:

$$r \approx \sqrt{x_p^2 + y_p^2 + z_i^2} - \frac{x_i x_p + y_i y_p}{z_i}, \tag{S5}$$

where a represents the radius of the aperture.

Ochoa's approximation can be obtained by substituting Eq. S5 into the exponential term (e^{jkr}) of Eq. S1, and replacing r by $r_n = \sqrt{x_p^2 + y_p^2 + z_i^2}$ in the denominators of Eq. S1a:

$$\begin{aligned} U(x_i, y_i, z_i) =& \frac{z_i}{2\pi}\iint_P \left[U(x_p, y_p, 0)\left(\frac{1}{r_n} - jk\right)\frac{e^{jkr_n}}{r_n^2}\right] \times e^{-j\frac{2\pi}{\lambda z_i}(x_i x_p + y_i y_p)} dx_p dy_p \\ =& \frac{z_i}{2\pi}\mathcal{F}\left[U(x_p, y_p, 0)\left(\frac{1}{r_n} - jk\right)\frac{e^{jkr_n}}{r_n^2}\right]\left(\frac{x_i}{\lambda z_i}, \frac{y_i}{\lambda z_i}\right). \end{aligned} \tag{S6}$$

The error of this approximation decreases as the f-number ($f/\#$) of the optical system increases [Ochoa 2017]. This parameter is expressed as:

$$f/\# = \frac{f}{2a}, \tag{S7}$$

where f and a respectively represent the focal length and the radius of the circular aperture causing diffraction.

S1.3 Fresnel Approximation

If $r \gg \lambda$, Eq. S1a can be simplified as [Goodman 2017]:

$$U(x_i, y_i, z_i) = \frac{z_i}{j\lambda}\iint_P U(x_p, y_p, 0)\frac{e^{jkr}}{r^2} dx_p dy_p. \tag{S8}$$

When the propagation distance d satisfies the condition:

$$d \gg \sqrt[3]{\frac{\pi}{4\lambda}[(x_i - x_p)^2 + (y_i - y_p)^2]_{max}^2}, \tag{S9}$$

where max refers to the maximum possible expression value given any valid (x_i, y_i, x_p, y_p), the parameter r (Eq. S1b) can be approximated by:

$$r \approx d\left[1 + \frac{1}{2}\left(\frac{x_i - x_p}{d}\right)^2 + \frac{1}{2}\left(\frac{y_i - y_p}{d}\right)^2\right]. \tag{S10}$$

The Fresnel approximation can then be obtained by substituting Eq. S10 into Eq. S8 [Goodman 2017]:

$$\begin{aligned} U(x_i, y_i, z_i) =& \frac{e^{jkz_i}}{j\lambda z_i} e^{j\frac{k}{2z_i}(x_i^2+y_i^2)} \iint_P \left[U(x_p, y_p, 0) e^{j\frac{k}{2z_i}(x_p^2+y_p^2)} \right] \times e^{-j\frac{2\pi}{\lambda z_i}(x_i x_p + y_i y_p)} dx_p dy_p \\ =& \frac{e^{jkz_i}}{j\lambda z_i} e^{j\frac{k}{2z_i}(x_i^2+y_i^2)} \mathcal{F}\left[U(x_p, y_p, 0) e^{j\frac{k}{2z_i}(x_p^2+y_p^2)} \right] \left(\frac{x_i}{\lambda z_i}, \frac{y_i}{\lambda z_i} \right). \end{aligned} \tag{S11}$$

We note that the Fresnel approximation was adopted by Ritschel et al. [2009] and Luidolt et al. [2020] to reproduce glare.

S1.4 Fraunhofer Approximation

If $z_i \gg \frac{k(x_p^2+y_p^2)_{max}}{2}$, then the propagation kernel $e^{j\frac{k}{2z_i}(x_p^2+y_p^2)}$ approaches to one. The Fraunhofer approximation can be obtained by removing the exponential term inside the Fourier transform of the Fresnel approximation (Eq. S11) [Goodman 2017]:

$$U(x_i, y_i, z_i) = \frac{e^{jkz_i}}{j\lambda z_i} e^{j\frac{k}{2z_i}(x_i^2+y_i^2)} \mathcal{F}[U(x_p, y_p, 0)] \left(\frac{x_i}{\lambda z_i}, \frac{y_i}{\lambda z_i} \right). \tag{S12}$$

We also note that the Fraunhofer approximation has been adopted by Kakimoto et al. [2004] to reproduce the glare.

S1.5 Fresnel and Fraunhofer Approximations

Kakimoto et al. [2004] proposed that the light wave on the image plane can be obtained by applying Fraunhofer diffraction on a given pupil or obstacles (represented as a mask) on the pupil plane. Ritschel et al. [2009] proposed the use of Fresnel diffraction to replace the former since it has higher physical accuracy. Considering the perfect focus setup described in Section. 4.1 (*i.e.*, $z_i = d = f$), by substituting Eq. 11 into Eq. S11, we obtain:

$$\begin{aligned} U(x_i, y_i, d) &\propto \mathcal{F}[U(x_p, y_p, 0) e^{j\frac{k}{2z_i}(x_p^2+y_p^2)}] \left(\frac{x_i}{\lambda d}, \frac{y_i}{\lambda d} \right) \\ &= \mathcal{F}[U_0(x_p, y_p, 0) \cdot P(x_p, y_p) \cdot t(x_p, y_p) e^{j\frac{k}{2z_i}(x_p^2+y_p^2)}] \left(\frac{x_i}{\lambda d}, \frac{y_i}{\lambda d} \right) \\ &= \mathcal{F}[U_0(x_p, y_p, 0) \cdot P(x_p, y_p) e^{j\frac{k-k}{2f}(x_p^2+y_p^2)}] \left(\frac{x_i}{\lambda d}, \frac{y_i}{\lambda d} \right) \\ &= \mathcal{F}[U_0(x_p, y_p, 0) \cdot P(x_p, y_p)] \left(\frac{x_i}{\lambda d}, \frac{y_i}{\lambda d} \right). \end{aligned} \tag{S13}$$

Eq. S13 shows that the point spread function (PSF) generated using the Fresnel approximation with perfect focused lens setup is equivalent to the PSF generated using the Fraunhofer approximation with the lens removed as indicated by Goodman [2017]. Therefore, we will treat these two approximations as the same propagation method and refer to them as the “Fresnel approximation" in this work.

S2 Brightness Mapping Function

In this section, we provide more details about the final step of our proposed visual response function. Initially, we denote the luminance mapped to reference white (display level 255) and the luminance mapped to reference black (display level 0) by $L^{refWhite}$ and $L^{refBlack}$, respectively. We then employ L^{env} to denote the luminance of the environment. Lastly, we use $L^{pattern}_{photopic}$ and $L^{pattern}_{scotopic}$ to denote the patterns' photopic luminance (associated with the cones) and scotopic luminance (associated with the rods), respectively.

The brightness values assigned to reference white, reference black, and the combination of pattern and environment stimuli are respectively calculated using the following expressions:

$$B^{refWhite} = B(L^{refWhite}, L^{refWhite}), \tag{S14}$$

$$B^{refBlack} = B(L^{refBlack}, L^{refBlack}), \tag{S15}$$

and

$$B^{pattern+env} = B(L^{pattern}_{photopic} + L^{env}, L^{pattern}_{scotopic} + L^{env}), \tag{S16}$$

where the function B represents the mapping from luminance to brightness (Eq. 16).

The color c assigned to $B^{pattern+env}$ is then defined through the following linear interpolation expression:

$$B^{pattern+env} = B^{refBlack} + c(B^{refWhite} - B^{refBlack}), \tag{S17}$$

which can be rewritten as:

$$\begin{aligned} c =& \frac{B^{pattern+env} - B^{refBlack}}{B^{refWhite} - B^{refBlack}} \\ =& \frac{B(L^{pattern}_{photopic} + L^{env}, L^{pattern}_{scotopic} + L^{env}) - B(L^{refBlack}, L^{refBlack})}{B(L^{refWhite}, L^{refWhite}) - B(L^{refBlack}, L^{refBlack})}. \end{aligned} \tag{S18}$$

Since B is monotonic and Eq. S18 is an inverse linear interpolation, if $L^{refBlack} \leq L_v \leq L^{refWhite}$, then $c \in [0, 1]$. Finally, Eq. 17 can be obtained by applying Eq. S18 for three color channels:

$$c_{LMS}[i] = \frac{B(L^{pattern}_{photopic}[i] + L^{env}[i], L^{pattern}_{scotopic}[i] + L^{env}[i]) - B(L^{refBlack}[i], L^{refBlack}[i])}{B(L^{refWhite}[i], L^{refWhite}[i]) - B(L^{refBlack}[i], L^{refBlack}[i])}, \tag{S19}$$

where LMS is the color space that represents the response of three types of cones [Banterle et al. 2018], with $i = 1, 2, 3$ representing each color component. Note that, in the main body of the article, we added a subscript v to each of the notations to emphasize that they are luminance in contrast to radiance. For formatting reasons, we also abbreviated $L^{pattern}_{photopic}$, $L^{pattern}_{scotopic}$, $L^{refBlack}_v$ and $L^{refWhite}_v$ to L^p_v, L^s_v, rB and rW, respectively, in the main text.

S3 Implementation Aspects

This section provides details on the representation of the wave plane and the implementation of the visual response function, including the overall setup, the software framework used, and the construction of luminance to brightness functions.

The light wave, as a core component of the propagation stage, is represented as a square matrix of size $2^h \times 2^h$ for some integer h with complex number entries. The physical size assigned to the matrix that represents the pupil plane is $8\ mm \times 8\ mm$. Note that for the direct Fast Fourier transform (FFT) implementations, we doubled the physical size of the plane to $16\ mm \times 16\ mm$ for better visual results (padding with zeros the rows and columns that become empty once the pupil representation inside the square matrix is reduced). The value of h was chosen to meet the requirement of sampling or the desired visual quality.

We implemented each approximation algorithm with NumPy and Diffractio [Sanchez-Brea et al. 2024] library, which provides routines that implement the RS diffraction with convolution and Chirp Z transform (CZT). To facilitate visual interaction, we implemented the response stage in a fragment shader with OpenGL [Kessenich et al. 2017] and adopted Dear ImGui [Cornut 2024] as the user interface.

Parameters	Photopic	Scotopic
k_a	6.311	2.168
k_b	10.441	1.135
k_c	11.373	0.004
k_d	0.122	22.552
k_e	3.471	4.091
k_f	-9.058	0.000
k_g	0.566	1.000
k_h	-12.916	13.395

Table S1. Parameter values used to obtain the photopic and scotopic fitted curves depicted in Fig. S1

For the choice of spectral luminous efficiencies, we adopted the CIE XYZ color matching function for cones ($V(\lambda)$) (convert to LMS color space and RGB color space afterwards), and CIE Scotopic luminosity curve for rods ($V'(\lambda)$) [Ohno et al. 2020].

The propagation results were generated for each wavelength of the spectrum region from 360 to 830 *nm*, and stored in OpenEXR format [Kainz et al. 2003]. Simulations were executed on a workstation with 128 GB RAM equipped with an AMD Ryzen 3990X.

The mapping function (Eq. 15) is data-driven and discrete, which makes it difficult to invert and accommodate continuous input. To address, we fitted the data with the following equation using *curve_fit* [Virtanen et al. 2020]:

$$y(x) = k_a x + k_b \log(k_c + k_d e^{k_e x}) + k_f e^{-k_g^2 x} + k_h, \tag{S20}$$

with the k parameters being assigned the values listed in Table. S1. We then plotted the fitted curve depicted in Fig. S1.

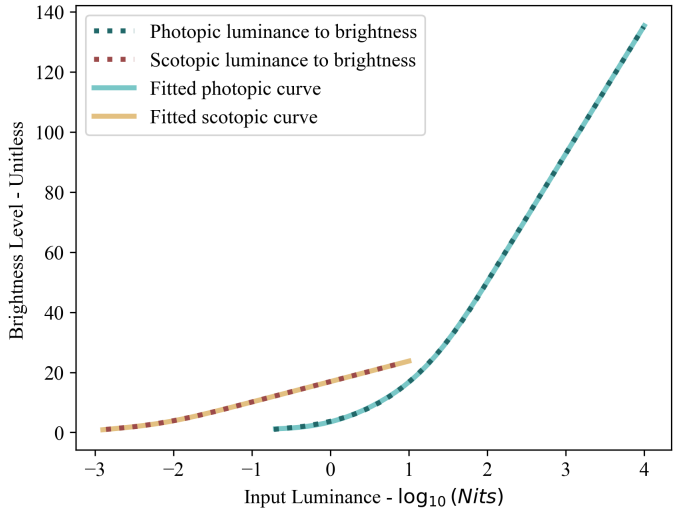

Fig. S1. Fitted curves for luminance to brightness mapping function (inverse of Eq. 15). Two solid curves are data-driven functions for photopic and scotopic cases. The dotted curves are fitted results obtained using Eq. S20 and the parameter values listed in Table S1.

S4 Time and Space Efficiency

In this section, we provide more quantitative details regarding the offline pre-computation of the point spread function (PSF) of the glare pattern. All propagation methods introduced in Section 3.2 and Chirp Z transform (CZT) were implemented using a constant number of FFT operations and their inverses. Thus, they all have time complexity $O(N^2 logN)$ and space complexity $O(N^2)$, where N is the number of rows of the square input matrix [Hu et al. 2020; Shen and Wang 2006]. We profiled the performance of these algorithms considering distinct values for N, and recorded the time consumption and peak memory usage in Table S2. Although the implementation affects the exact performance, the asymptotic trends of time and space matched the theoretical complexities outlined earlier. Furthermore, as expected, the algorithms that employed FFT were faster than those that used CZT since CZT operations were implemented with two FFT operations and one inverse Fast Fourier transform (iFFT) operation.

Note that when the input matrix size increases by a factor of 4 (from 4096 to 16384) in a Fresnel diffraction execution employing FFT, the memory usage increases by a factor of 16, growing from 2.82 GB to 45.07 GB. This is because the matrix size is a one-dimensional measure, whereas memory usage scales with two-dimension. Furthermore, we observe that with the FFT-based implementation, Ochoa's approximation is approximately 6× faster than the reference solution, whereas the Fresnel approximation is only about 3× faster. This difference is mainly due to the fact that the Fresnel approximation formula (Eq. S11) contains a coefficient whose computation requires a markedly larger number of floating point operations than that of Ochoa's approximation (Eq. S6).

It is also worth noting that Ochoa's approximation produces results that approximate the reference patterns (obtained using the RS diffraction solution) more closely than those produced by the Fresnel approximation. Moreover, the computational time associated with Ochoa's approximation is lower than that associated with the Fresnel approximation. For these reasons, we suggest the use of Ochoa's approximation, instead of the Fresnel approximation, in the generation of the glare patterns discussed in this work.

Table S2. Time and peak memory costs. Matrix size refers to the size of the 2D matrix that represents waves. $Time_T$ is the time spent in executing of the propagation stage. $Time_R$ refers to the time to scale the propagation results to a specific size. This metric is only available for FFT implementations as CZT is capable of generating a matrix representing the image plane with a user-selected physical size. Memory usage corresponds to the peak usage during the whole execution procedure.

Rayleigh-Sommerfeld diffraction with Fast Fourier transform			
Matrix Size	$Time_T$	$Time_R$	Memory Usage
16384	288.95s	233.86s	106.50 GB
Ochoa's approximation with Fast Fourier transform			
Matrix Size	$Time_T$	$Time_R$	Memory Usage
1024	0.08s	0.22s	0.17 GB
4096	2.83s	10.88s	2.69 GB
16384	46.34s	285.10s	43.02 GB
Fresnel diffraction with Fast Fourier transform			
Matrix Size	$Time_T$	$Time_R$	Memory Usage
1024	0.12s	0.22s	0.19 GB
4096	6.53s	10.94s	2.82 GB
16384	95.22s	286.42s	45.07 GB
Ochoa's approximation with Chirp Z transform			
Matrix Size	$Time_T$	$Time_R$	Memory Usage
1024	0.25s	N/A	0.27 GB
4096	8.96s	N/A	4.36 GB
16384	152.23s	N/A	69.65 GB
Fresnel diffraction with Chirp Z transform			
Matrix Size	$Time_T$	$Time_R$	Memory Usage
1024	0.27s	N/A	0.28 GB
4096	9.15s	N/A	4.35 GB
16384	157.45s	N/A	69.63 GB

S5 Photographics Illustration of Glare Scenarios

In this section, we present two sequences of photos depicting scenarios appropriate for the observation of the glare phenomenon, and briefly comment on the shortcomings of using photographs in the evaluation of computer-generated glare patterns.

The photos were taken using a Sony ILCE7RM5 camera with a Tamron A063 lens. In Fig. S2, we present a sequence of photos depicting a nighttime scene. These photos were taken varying the following camera parameters:

- aperture ($f/\# = f/2.8, f/5.6, f/11, f/22$) and
- sensitivity ($ISO = 100, 320, 1250, 3200$).

The remaining parameters, focal length and exposure time, were kept as $f = 75\ mm$ and $t = 2.5\ s$, respectively.

(a) (b)

(c) (d)

Fig. S2. A sequence of photos taken by a camera during nighttime to show the camera version of glare patterns. The patterns could be observed around the headlights. The photos presented in Figs. (a), (b), (c), and (d) correspond to aperture sizes $f/\#$ equal to $f/2.8, f/5.6, f/11$, and $f/22$, respectively.

In Fig. S3, we present a sequence of photos depicting a daytime scene. These photos were taken varying the following camera parameters:

- aperture ($f/\# = f/2.8, f/5.6, f/11, f/22$),

- exposure time ($t = 1/1000\ s, 1/400\ s, 1/100\ s, 1/25\ s$) and
- sensitivity ($ISO = 100, 100, 125, 100$).

The focal length was kept as $f = 75\ mm$.

(a) (b) (c) (d)

Fig. S3. A sequence of photos taken by a camera during daytime to show the camera version of glare patterns. The patterns could be observed around the specular reflection spots. The photos presented in Figs. (a), (b), (c), and (d) correspond to aperture sizes $f/\#$ equal to $f/2.8$, $f/5.6$, $f/11$, and $f/22$, respectively.

Note that although some spikes can be observed in the photos presented in Figs. S2 and S3, the photographic depiction of the phenomenon cannot fully capture its visual richness as perceived by a human observer through the human visual system (HVS). This limitation may be attributed to the presence of biological microstructures, which can diffract light, on the human crystalline lens [Ritschel et al. 2009]. The lens of a camera imaging system, on the other hand, has no structural irregularities under normal manufacturing conditions.

It is worth noting that the patterns observed on the photographs resulted from the diffraction that occurred at the edge of the aperture in a camera lens system [Hullin et al. 2011]. In our work, however, we simulate the patterns resulting from the diffraction caused by particles (representing biological microstructures) on the human crystalline lens [Ritschel et al. 2009]. Due to the distinct characteristics of the human eye and a camera's optical system (*e.g.*, lens

with less imperfections), the latter cannot produce the same depictions of glare patterns perceived by human observers. We note that these patterns contain more spikes than the patterns captured in the photographs.

While the HVS has photosensitive cells, cones and rods, (digital) cameras use filters (*e.g.,* Bayer filter [Maître 2015]) in conjunction with a CMOS (Complementary Metal Oxide Semiconductor) sensor [Maître 2015] to convert light to colors. Such functionality is similar to the HVS's photopic sensitivity (associated with the cone cells). The lack of scotopic sensitivity (associated with rod cells) makes the cameras unable to capture the correct colors of nighttime scenes. Also, their relatively limited dynamic range prevents them from capturing all the spike details (associated with the contrast between the spikes and the background) of the glare patterns. For example, if a camera's exposure level is set based on the intensity of a light source, the camera's limited dynamic range may underexpose dark areas, leading to a loss of these details. In this case, the spikes would appear unrealistically less discernible from their surroundings.

In short, the patterns observed in photos result from diffraction taking place at the edge of the aperture of a camera's lens system, while glare patterns observed by the naked eye result from biological microstructures (particles) on the crystalline lens. Such differences hinder the evaluation of computer-generated depictions of glare patterns through direct comparisons with photos attempting to capture them as they are perceived by a human observer.

S6 Light Source Impact on Glare Patterns

In this section, we show that the spectral power distribution (SPD) of the light source would affect the visual appearance of the pattern. Simpson [1953] has mentioned that glare-related patterns seen under monochromatic light are different from those seen under white light as they break up into a large number of spots. Furthermore, van den Berg et al. [2005] have stated that the radiating line in the chromatic PSF (*e.g.*, Figs. S4a and S4b) arises from the alignment of spots in each monochromatic PSF (*e.g.*, Fig. S4d) for different wavelengths. Thus, for our simulations, we selected four types of light sources based on their SPDs:

- light source with uniform SPD as the base case,
- standard illuminant D65 [CIE 2022], which has smooth SPD,
- CIE fluorescent lamp #23, which contains a few peaks in its SPD, and
- red light-emitting diode (LED) light whose SPD consists of a single peak.

As it can be observed in Fig. S4, the pattern obtained using the D65 illuminant has spikes similar to those in the pattern obtained considering the light source with uniform SPD, but a different color. In contrast, the pattern obtained considering the fluorescent lamp fails to form a spike in its PSF since its SPD consists of only a few peaks. Furthermore, the pattern obtained using the red LED consists of discrete red dots since the SPD of the red LED only has a single peak.

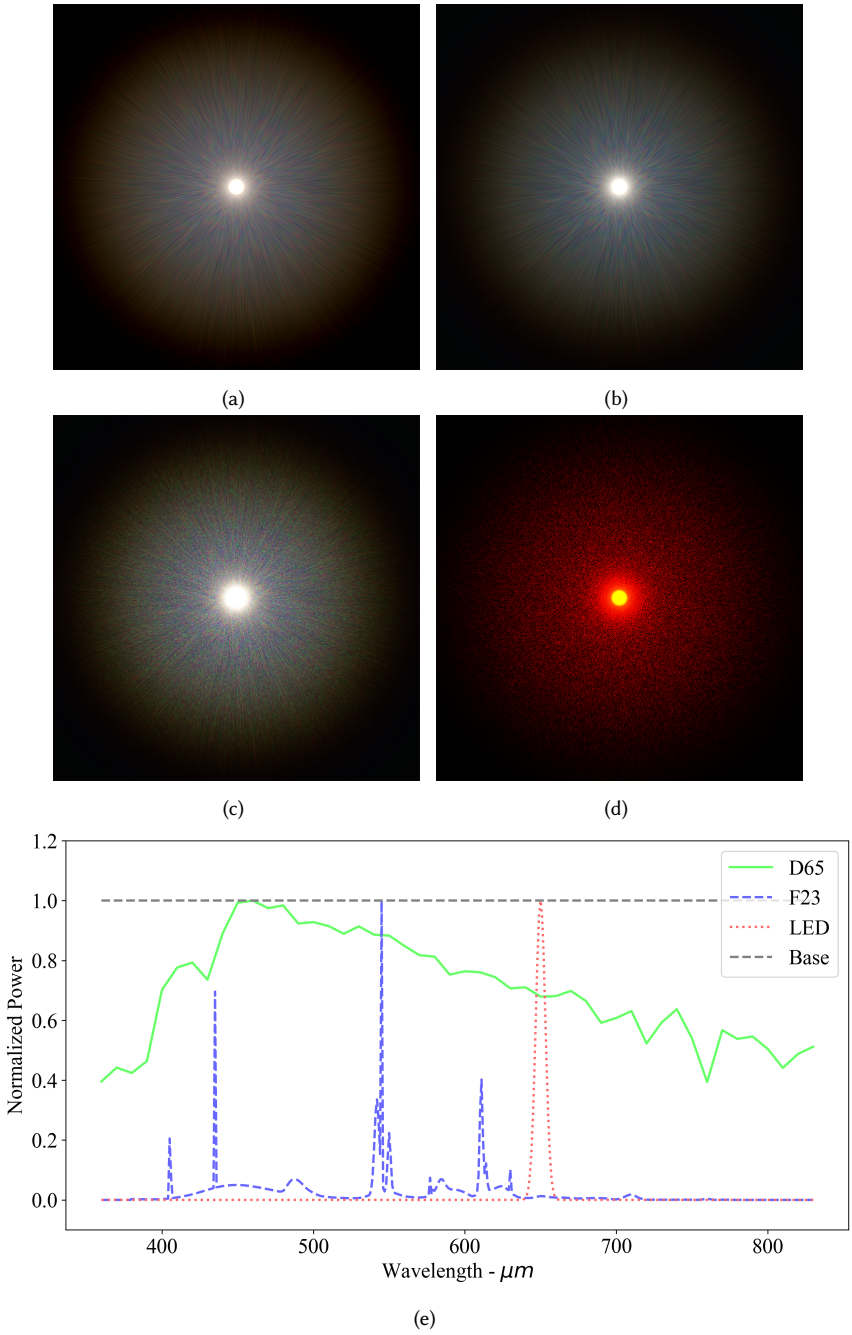

Fig. S4. Glare patterns generated using the proposed framework and considering different light sources. (a) Light source with uniform SPD. (b) CIE D65 illuminant. (c) CIE Fluorescent lamp (F23). (d) Red LED approximated with Gaussian distribution ($\mu = 650\ nm, \sigma = 20\ nm$). (e) Relative spectral power distributions of the light sources used in (a), (b) [CIE 2022], (c) [CIE 2018], and (d). From (a) to (d), the SPDs of the light sources shift to a peak distribution from a smooth distribution, and the corresponding pattern shifts from spikes to discrete dots.

References

Francesco Banterle, Alessandro Artusi, Kurt Debattista, and Alan Chalmers. 2018. *Advanced High Dynamic Range Imaging* (second ed.). Taylor & Francis, CRC Press, Boca Raton.

Omar Cornut. 2024. Dear ImGui. https://github.com/ocornut/imgui Published: GitHub repository.

Joseph W. Goodman. 2017. *Introduction to Fourier Optics* (fourth ed.). W.H. Freeman, Macmillan Learning, New York.

Yanlei Hu, Zhongyu Wang, Xuewen Wang, Shengyun Ji, Chenchu Zhang, Jiawen Li, Wulin Zhu, Dong Wu, and Jiaru Chu. 2020. Efficient full-path optical calculation of scalar and vector diffraction using the Bluestein method. *Light: Science & Applications* 9, 1 (July 2020), 119. doi:10.1038/s41377-020-00362-z

Matthias Hullin, Elmar Eisemann, Hans-Peter Seidel, and Sungkil Lee. 2011. Physically-based real-time lens flare rendering. In *ACM SIGGRAPH 2011*. ACM, Vancouver British Columbia Canada, 1–10. doi:10.1145/1964921.1965003

International Commission On Illumination (CIE). 2018. *Relative spectral power distributions of illuminants representing typical fluorescent lamps, 1nm wavelength steps.* Technical Report CIE 2018. CIE, Vienna, Austria. doi:10.25039/CIE.DS.54hy6srn

International Commission On Illumination (CIE). 2022. *CIE standard illuminant D65.* Technical Report CIE 2022. CIE, Vienna, Austria. doi:10.25039/CIE.DS.hjfjmt59

Florian Kainz, Rod Bogart, and Drew Hess. 2003. The OpenEXR image file format. *ACM SIGGRAPH Technical Sketches* 2 (2003), 26.

Masanori Kakimoto, Kaoru Matsuoka, Tomoyuki Nishita, Takeshi Naemura, and Hiroshi Harashima. 2004. Glare Generation Based on Wave Optics. In *Proceedings of the Computer Graphics and Applications, 12th Pacific Conference (PG '04)*. IEEE Computer Society, USA, 133–142.

John M. Kessenich, Graham Sellers, and Dave Shreiner. 2017. *OpenGL programming guide: the official guide to learning OpenGL, version 4.5 with SPIR-V* (ninth edition ed.). Addison-Wesley, Boston, MA.

Laura R. Luidolt, Michael Wimmer, and Katharina Krosl. 2020. Gaze-dependent simulation of light perception in virtual reality. *IEEE Transactions on Visualization and Computer Graphics* 26, 12 (Dec. 2020), 3557–3567. doi:10.1109/TVCG.2020.3023604

Henri Maître. 2015. *From photon to pixel: the digital camera handbook.* John Wiley & Sons, Inc, Hoboken, NJ. doi:10.1002/9781119238447

Noé Alcalá Ochoa. 2017. Alternative approach to evaluate the Rayleigh-Sommerfeld diffraction integrals using tilted spherical waves. *Optics Express* 25, 10 (May 2017), 12008. doi:10.1364/OE.25.012008

Yoshi Ohno, Teresa Goodman, Peter Blattner, Janos Schanda, Hiroshi Shitomi, Armin Sperling, and Joanne Zwinkels. 2020. Principles Governing Photometry (2nd edition). *Metrologia* 57, 2 (April 2020), 020401. doi:10.1088/1681-7575/ab72f1

T. Ritschel, M. Ihrke, J. R. Frisvad, J. Coppens, K. Myszkowski, and H.-P. Seidel. 2009. Temporal glare: real-time dynamic simulation of the scattering in the human eye. *Computer Graphics Forum* 28, 2 (April 2009), 183–192. doi:10.1111/j.1467-8659.2009.01357.x

Luis Miguel Sanchez-Brea, Angela Soria-Garcia, Joaquin Andres-Porras, Veronica Pastor-Villarrubia, Mahmoud H. Elshorbagy, Jesus Del Hoyo, Francisco Jose Torcal-Milla, and Javier Alda. 2024. Diffractio: an open-source library for diffraction and interference calculations. In *Optics and Photonics for Advanced Dimensional Metrology III*, Peter J. De Groot, Pascal Picart, and Felipe Guzman (Eds.). SPIE, Strasbourg, France, 46. doi:10.1117/12.3021879

Fabin Shen and Anbo Wang. 2006. Fast-Fourier-transform based numerical integration method for the Rayleigh-Sommerfeld diffraction formula. *Applied Optics* 45, 6 (Feb. 2006), 1102. doi:10.1364/AO.45.001102

G. C. Simpson. 1953. Ocular haloes and coronas. *British Journal of Ophthalmology* 37, 8 (Aug. 1953), 450–486. doi:10.1136/bjo.37.8.450

Thomas J. T. P. van den Berg, Michiel P. J. Hagenouw, and Joris E. Coppens. 2005. The ciliary corona: physical model and simulation of the fine needles radiating from point light sources. *Investigative Opthalmology & Visual Science* 46, 7 (July 2005), 2627. doi:10.1167/iovs.04-0935

Pauli Virtanen, Ralf Gommers, Travis E. Oliphant, Matt Haberland, Tyler Reddy, David Cournapeau, Evgeni Burovski, Pearu Peterson, Warren Weckesser, Jonathan Bright, Stéfan J. van der Walt, Matthew Brett, Joshua Wilson, K. Jarrod Millman, Nikolay Mayorov, Andrew R. J. Nelson, Eric Jones, Robert Kern, Eric Larson, C. J. Carey, İlhan Polat, Yu Feng, Eric W. Moore, Jake VanderPlas, Denis Laxalde, Josef Perktold, Robert Cimrman, Ian Henriksen, E. A. Quintero, Charles R. Harris, Anne M. Archibald, Antônio H. Ribeiro, Fabian Pedregosa, Paul van Mulbregt, Aditya Vijaykumar, Alessandro Pietro Bardelli, Alex Rothberg, Andreas Hilboll, Andreas Kloeckner, Anthony Scopatz, Antony Lee, Ariel Rokem, C. Nathan Woods, Chad Fulton, Charles Masson, Christian Häggström, Clark Fitzgerald, David A. Nicholson, David R. Hagen, Dmitrii V. Pasechnik, Emanuele Olivetti, Eric Martin, Eric Wieser, Fabrice Silva, Felix Lenders, Florian Wilhelm, G. Young, Gavin A. Price, Gert-Ludwig Ingold, Gregory E. Allen, Gregory R. Lee, Hervé Audren, Irvin Probst, Jörg P. Dietrich, Jacob Silterra, James T. Webber, Janko Slavič, Joel Nothman, Johannes Buchner, Johannes Kulick, Johannes L. Schönberger, José Vinícius de Miranda Cardoso, Joscha Reimer, Joseph Harrington, Juan Luis Cano Rodríguez, Juan Nunez-Iglesias, Justin Kuczynski, Kevin Tritz, Martin Thoma, Matthew Newville, Matthias Kümmerer, Maximilian Bolingbroke, Michael Tartre, Mikhail Pak, Nathaniel J. Smith, Nikolai Nowaczyk, Nikolay Shebanov, Oleksandr Pavlyk, Per A. Brodtkorb, Perry Lee, Robert T. McGibbon, Roman Feldbauer, Sam Lewis, Sam Tygier, Scott Sievert, Sebastiano Vigna, Stefan Peterson, Surhud More, Tadeusz Pudlik, Takuya Oshima, Thomas J. Pingel, Thomas P. Robitaille, Thomas Spura, Thouis R. Jones, Tim Cera, Tim Leslie, Tiziano Zito, Tom Krauss, Utkarsh Upadhyay, Yaroslav O. Halchenko, Yoshiki Vázquez-Baeza, and SciPy 1.0 Contributors. 2020. SciPy 1.0: fundamental algorithms for scientific computing in Python. *Nature Methods* 17, 3 (March 2020), 261–272. doi:10.1038/s41592-019-0686-2